J. Fluid Mech. (2025), *vol.* 1019, R5, doi:10.1017/jfm.2025.10621

The influence of Langmuir circulation and its modulation by an oscillating along-shelf current on the dynamics of cross-shelf flows

Thathsarani D.H. Herath Mudiyanselage[1], **J.J. Peñaloza-Gutierrez**[2], **Boris Galperin**[3], **Cigdem Akan**[4] **and Andrés Eligio Tejada-Martínez**[1]

[1]Civil & Environmental Engineering, University of South Florida, Tampa, FL, USA

[2]Mechanical Engineering, University of South Florida, Tampa, FL, USA

[3]College of Marine Science, University of South Florida, St. Petersburg, FL, USA

[4]Geospatial Research Laboratory, U.S Army Engineer Research and Development Center, Alexandria, VA, USA

Corresponding author: Thathsarani D.H. Herath Mudiyanselage, thathsaranid@usf.edu

(Received 16 June 2025; revised 29 July 2025; accepted 19 August 2025)

Cross-shelf transport in the inner continental shelf is governed by wind, wave and tidal interactions, but the role of Langmuir circulation (LC), induced by wave–current interaction and modulated by tides, has remained under-studied in this setting. We develop a Reynolds-averaged Navier–Stokes (RANS) model incorporating the Craik–Leibovich vortex force to resolve LC, coupled with a mass-conserving undertow and oscillating along-shelf tidal currents, and compare results against field data from the Martha's Vineyard Coastal Observatory (MVCO). Under strong wave forcing (significant wave height $H_{sig} = 2.12$ m and significant wave period $T_w = 5.8$ s), LC persists throughout the tidal cycle, reducing vertical shear in the tidally averaged cross-shelf velocity profile compared with simulations excluding LC. During peak tidal velocity (reaching 25 cm s^{-1} with period of 12.42 h), LC is temporarily suppressed but reforms rapidly as tidal energy declines, sustaining high vertical mixing. Conversely, under weak wave forcing ($H_{sig} = 0.837$ m, $T_w = 4.3$ s), tidal currents persistently suppress LC, resulting in a cross-shelf undertow profile with greater vertical shear compared with strong-wave conditions. Model–observation comparisons show that only simulations including both the Craik–Leibovich vortex force and tidal forcing reproduce the observed undertow structure at MVCO. These results demonstrate that accurate prediction of cross-shelf transport at tidal and subtidal time scales requires resolving both the generation and disruption of LC by tides.

Key words: wind-wave interactions, ocean processes, turbulence modelling

1. Introduction

Cross-shelf flows regulate the transport of heat, nutrients and biogenic materials, shaping both coastal ecosystems and broader oceanographic processes. These exchanges link the surf zone to the mid-shelf, influencing biological productivity and physical circulation patterns. However, predicting cross-shelf transport remains a challenge due to the complex interactions among surface winds, waves and bottom stresses (Lentz & Fewings 2012).

Langmuir circulation (LC), a byproduct of wind–wave interaction, plays a crucial role in enhancing vertical mixing, redistributing turbulent kinetic energy (TKE), momentum and scalars throughout the water column (Thorpe 2004). LC has been shown to be an important process in the inner shelf (Gargett *et al.* 2004). However, its influence on other key processes, particularly interactions with tidal currents and impacts on cross-shelf transport, remains poorly understood.

While along-shelf winds are wellestablished as primary drivers of mid-shelf circulation, cross-shelf wind stress and wave forcing become dominant in the inner shelf. Historically, cross-shelf wind stress was considered negligible in along-shelf circulation studies, leading to its omission from many numerical models. However, recent observations suggest that in shallow waters ($\leqslant$30 m), cross-shelf wind stress plays a leading role in the cross-shelf momentum balance (Lentz & Fewings 2012).

At Martha's Vineyard Coastal Observatory (MVCO), in a water column 12 m in depth, Fewings, Lentz & Fredericks (2008) observed a marked reduction in vertical shear of the offshore-directed undertow during periods of strong onshore winds and waves, suggesting enhanced vertical mixing that may be linked to LC.

It is hypothesised that the wave- and wind-driven LC could be the source of the vertical mixing of undertow momentum observed by Fewings *et al.* (2008). To test this hypothesis, we develop a Reynolds-averaged numerical model that includes the Craik–Leibovich (C–L) vortex force to resolve LC and its modulation by the cross-wind tidal forcing observed at MVCO.

Recent modelling advancements have improved the representation of wave-driven inner-shelf processes (Warner *et al.* 2008; Uchiyama, McWilliams & Shchepetkin 2010). For example, Uchiyama *et al.* (2010) investigated wave–current interactions in cross-shelf flows but did not resolve wind- and wave-driven LC explicitly, instead focusing on the inclusion of parameterised representations of processes such as wave breaking and wave streaming. Furthermore, these studies have primarily considered subtidal time scales, which do not resolve the variability of LC and its modulation by tides. Given that tides are known to disrupt LC (Kukulka *et al.* 2011; Savidge & Gargett 2017), it is essential to examine LC within a tidal framework to fully capture its role in cross-shelf transport.

A one-dimensional (single water column) model was developed by Fewings *et al.* (2008) to represent wind- and wave-driven cross-shelf currents. Although this model achieved good agreement with field observations of the subtidal undertow at MVCO, it does not resolve the wave–current interaction responsible for LC and its associated vertical mixing of momentum. Instead, the reduced shear observed at MVCO during periods of both strong onshore winds and waves is achieved through the linear superposition of two uncoupled components: a wind-driven component, and a prescribed offshore-directed component that balances the onshore-directed Stokes drift mass flux.

The present study builds on the model developed by Fewings *et al.* (2008) by incorporating wave–current interaction that gives rise to LC, and further extending the framework to include the effects of tides. Comparisons with MVCO observations suggest that the modelled LC–tide interactions reproduce the vertical structure of the undertow. These results support the hypothesis that LC plays a central role in setting the vertical momentum distribution in cross-shelf flows.

2. Baseline model

The governing flow equations and computational set-up in this study are an extension of the model of Fewings *et al.* (2008), which predicts cross-shelf velocity profiles under combined onshore winds and waves. Their approach assumes that the Eulerian velocity response to these forcings can be represented as a linear superposition of two independent components: one driven by wind stress and the other by wave forcing. The wind-driven component follows the formulation of Lentz (1995), while the wave-driven component is based on the Hasselmann (1970) undertow model, which accounts for the offshore-directed compensatory flow balancing the onshore waves' Stokes drift transport. The velocity profile under combined forcing is expressed as

$$u_{\tau+H} = u_\tau + u_H, \tag{2.1}$$

where u_τ is the onshore wind-driven flow, and u_H is the offshore wave-driven undertow. The latter is assumed to be equal in magnitude and opposite in sign to the onshore Stokes drift velocity, expressed as

$$u_H = -U_1^S. \tag{2.2}$$

The Stokes drift velocity used by Fewings *et al.* (2008) is given by

$$U_1^S = \frac{gkH_{sig}^2}{8c}\frac{\cosh(2kx_3)}{\sinh^2(kH)}, \tag{2.3}$$

where the acceleration due to gravity is g, wavenumber is k, the significant wave height is H_{sig}, phase speed is c, water column depth is H, and distance above the bottom is x_3.

The Fewings *et al.* (2008) model employs the formulation of Lentz (1995) to numerically solve the steady-state, depth-dependent momentum equations for u_τ. The onshore-directed cross-shelf wind stress, τ, is applied as a surface boundary condition, while the bottom stress is parameterised using a quadratic drag law. A no-slip boundary condition is imposed at the bottom, ensuring zero velocity at the seabed. The model is solved for a range of eddy viscosity profiles, including constant, bilinear, bilinear cutoff and cubic profiles, to assess their impact on the velocity distribution.

A key feature of the Fewings *et al.* (2008) model for u_τ is an offshore pressure gradient accounting for zero net transport across the coastal boundary. This constraint requires that while the wind-driven flow in the surface layer moves in the direction of the wind, a compensatory return flow occurs in the lower water column to maintain mass balance.

A net zero cross-shelf mass flow in the u_τ component together with (2.2) implies that the cross-shelf mass flow of the total Eulerian velocity in (2.1) is directed offshore and is equal to the Stokes drift mass flow, thus

$$\int_0^H u_{\tau+H}\,\mathrm{d}x_3 = -\int_0^H U_1^S\,\mathrm{d}x_3. \tag{2.4}$$

The previously described model is designed for subtidal time scales as it does not resolve tidal variability. Furthermore, it does not account for wave–current interactions, thereby neglecting the generation of LC. Despite this limitation, the model provides a good approximation for the subtidal-scale cross-shelf transport observed at MVCO, as was described in the Introduction.

3. Present model: governing equations

The flow equations consist of the incompressible Reynolds-averaged continuity equation in (3.1) and momentum equations in (3.2):

$$\frac{\partial \langle u_i \rangle}{\partial x_i} = 0, \tag{3.1}$$

$$\frac{\partial \langle u_i \rangle}{\partial t} + \langle u_j \rangle \frac{\partial \langle u_i \rangle}{\partial x_j} = -\frac{\partial \langle \Pi \rangle}{\partial x_i} + \nu \frac{\partial^2 \langle u_i \rangle}{\partial x_j^2} - \frac{\partial \langle u_i' u_j' \rangle}{\partial x_j} + \epsilon_{ijk} U_j^S \langle \omega_k \rangle + g_{utow} \delta_{i1} + g_{tide} \delta_{i2}. \tag{3.2}$$

In these equations, brackets denote Reynolds averaging, and the ith component of the Reynolds-averaged Eulerian velocity is $\langle u_i \rangle$. The fluctuating component is u_i'. Alongwind, crosswind and vertical directions are denoted by x_1, x_2 and x_3, respectively, time is t, and the molecular kinematic viscosity is ν. The Levi–Civita symbol is ϵ_{ijk} and δ_{ij} is the Kronecker delta. Here, Π denotes the modified pressure, defined in terms of the mean pressure and the Stokes drift (McWilliams *et al.* 1997).

To account for the effect of waves on the wind-driven velocity the C–L vortex force, represented by $\epsilon_{ijk} U_j^s \langle \omega_k \rangle$, was included. This term represents the interaction between the Stokes drift velocity U_j^s of the waves and the mean vorticity $\langle \omega_k \rangle$ generated by the wind stress, capturing the wave–current interaction responsible for driving LC.

The Stokes drift velocity U_i^S is defined as $(U_1^S, 0, 0)$ where U_1^S is defined in (2.3).

Linked to the C–L vortex force is a revised pressure formulation which is given by McWilliams, Sullivan & Moeng (1997), and omitted here for brevity.

The body force g_{utow} is adjusted dynamically to drive the undertow component of the flow in the offshore x_1-direction such that

$$\int_0^H \langle u_1 \rangle \mathrm{d}x_3 = -\int_0^H U_1^S \mathrm{d}x_3, \tag{3.3}$$

consistent with (2.4). This approach differs from Fewings *et al.* (2008) in how the offshore-directed undertow is enforced. While Fewings *et al.* (2008) assume that the Eulerian offshore velocity is exactly equal in magnitude and opposite in sign to the Stokes drift (recall the baseline model in § 2), our approach introduces a body force that dynamically drives an offshore-directed mass flux equal to the Stokes drift transport. This formulation aligns with the methodology of Lentz *et al.* (2008), who use a depth-independent body force to ensure a consistent offshore return flow while allowing for more flexibility in the velocity profile.

A time-dependent tidal current oscillating between the positive and negative crosswind directions is imposed via the body force

$$g_{tide} = U_m \frac{2\pi}{T} \sin\left(\frac{2\pi t}{T}\right), \tag{3.4}$$

where U_m is maximum tidal current velocity at the top of the water column and T is the period.

In the present study, Coriolis forcing is omitted to maintain consistency with the simplified inner-shelf framework of Fewings *et al.* (2008). To verify this, we reproduced the wind-driven flow component, u_τ, in the model of Fewings *et al.* (2008) in (2.1), with and without Coriolis forcing and found that the resulting velocity profiles were nearly indistinguishable.

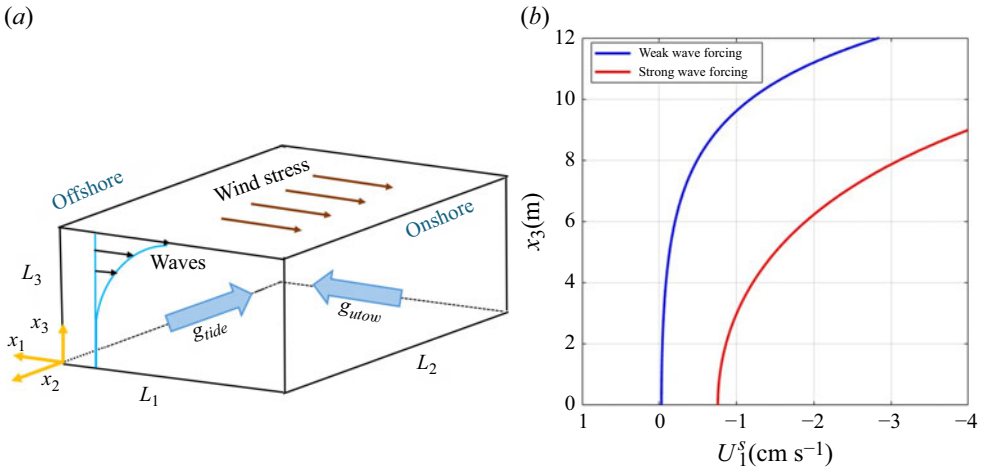

Figure 1. (*a*) Schematic of the computational domain forced by winds, waves and tides, and (*b*) Stokes drift profiles under strong and weak wave forcing.

The Reynolds stress in the momentum equation (3.2) , $-\langle u_i' u_j' \rangle$, is modelled following the classical k–ϵ closure (with k the turbulent kinetic energy and ϵ its dissipation rate) modified to account for production of TKE by Stokes drift velocity shear and non-local transport induced by LC, as shown in Perez *et al.* (2021) and Penaloza-Gutierrez *et al.* (2024) .

4. Computational set-up

The computational domain represents a uniform-depth water column, uninterrupted by lateral boundaries. Figure 1(*a*) provides a schematic of the domain used in the simulations, where L_1, L_2 and L_3 (or H) are the alongwind, crosswind and vertical domain dimensions, respectively.

The upper boundary of the domain is characterised by a wind-sheared rigid lid, while the bottom boundary is a no-slip wall. Periodic boundary conditions are imposed along both the alongwind (cross-shelf) and crosswind (cross-shelf) directions.

The depth of the water column ($H = 12$ m) has been chosen following the MVCO field measurements reported by Fewings *et al.* (2008). The length of the domain in the crosswind direction (62.8 m) has been chosen to resolve at least two pairs of Langmuir cells (Perez *et al.* 2021; Penaloza-Gutierrez *et al.* 2024).

The computational mesh includes 78 points in the vertical, 65 points in the crosswind, and 5 points in the alongwind directions, resulting in a total of 25 350 grid points.

The length of the longitudinal domain is arbitrary and has been discretised with only 5 points, since the representation of Langmuir cells in the current Reynolds-averaged Navier–Stokes (RANS) approach has been assumed to be two-dimensional (Perez *et al.* 2021; Penaloza-Gutierrez *et al.* 2024). This is consistent with the fact that Langmuir cells are generally aligned in the downwind direction (Thorpe 2004).

The body force g_{tide} generates a tidal current oriented in the crosswind, oscillating between positive and negative directions. This force approximates the tidal velocity dominated by the M2 tide reported at MVCO by Fewings *et al.* (2008), which has a significant along-shelf component (U_m) reaching 25 cm s^{-1} with a 12.42h period (T) (recall (3.4)).

Two wave forcing scenarios from the MVCO observations by Fewings *et al.* (2008) were considered. The first scenario represents weak wave forcing, with significant wave

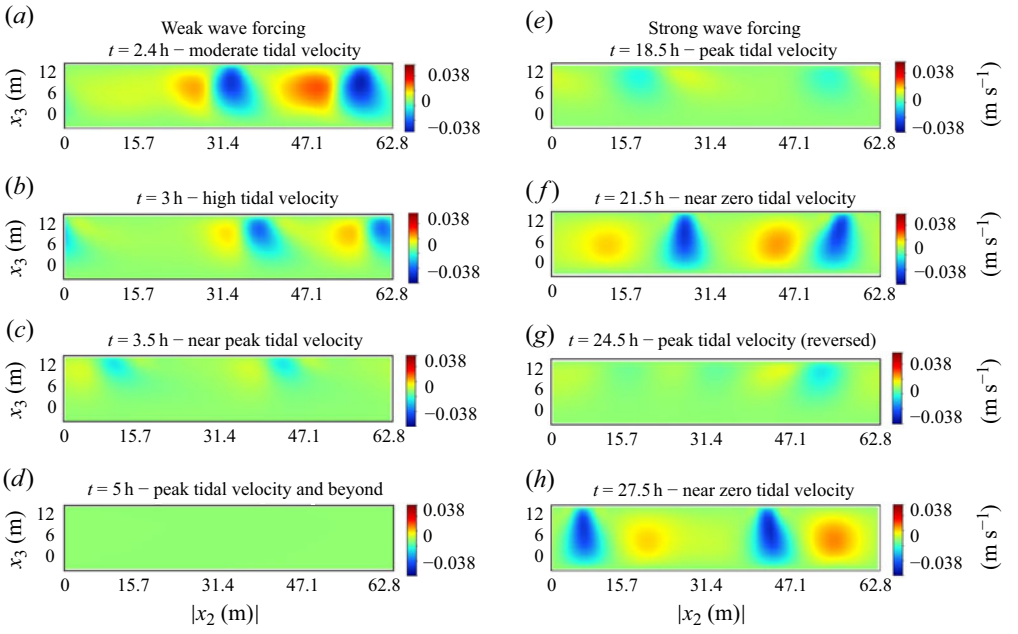

Figure 2. Vertical velocity fluctuations for weak wave forcing (*a–d*) and strong wave forcing (*e–h*) in the RANS simulation displayed on the crosswind–vertical plane.

height $H_{sig} = 0.837$ m, wave period $T_w = 4.3$ s, wavenumber $k = 0.2198$ m^{-1} (wavelength $\lambda = 28.6$ m) and wave speed $c = 6.645$ m s^{-1}. The second scenario corresponds to strong wave forcing, with $H_{sig} = 2.12$ m and $T_w = 5.8$ s, $k = 0.1305$ m^{-1} (wavelength $\lambda = 48.15$ m) and $c = 8.299$ m s^{-1}. These parameters determined the Stokes drift in (2.3) and the undertow body force, g_{utow}, in (3.2). The Stokes drift velocity in these scenarios are shown in figure 1(*b*). In both scenarios, a wind stress of 0.15 Pa was applied (corresponding to a 10 m wind speed of approximately 9.7 m s^{-1}).

The RANS equations for continuity and momentum were solved using the finite volume method (FVM). A staggered grid system was employed, spatially separating pressure and velocity points to enhance numerical stability and accuracy. A second-order upwind scheme was utilised for the discretisation of the momentum, TKE and TKE dissipation transport equations.

5. Results

Simulations were run starting from rest. Figure 2 shows the structure of the Langmuir cell in terms of vertical velocity contours in the crosswind–vertical plane of the computational domain at various times throughout simulations with weak and strong wave forcing. In this figure, at times when LC was active, the LC cells could be identified through pairs of downwelling and upwelling limbs, or regions of negative and positive vertical velocity, respectively.

5.1. *Weak wave forcing*

In the weak-wave-forcing case, LC formed during an initial transient period but over time was fully suppressed by the developing tidal current. This can be seen in figure 2(*a–d*) as well as in figure 3(*a*) in terms of the depth-average of the velocity variance versus

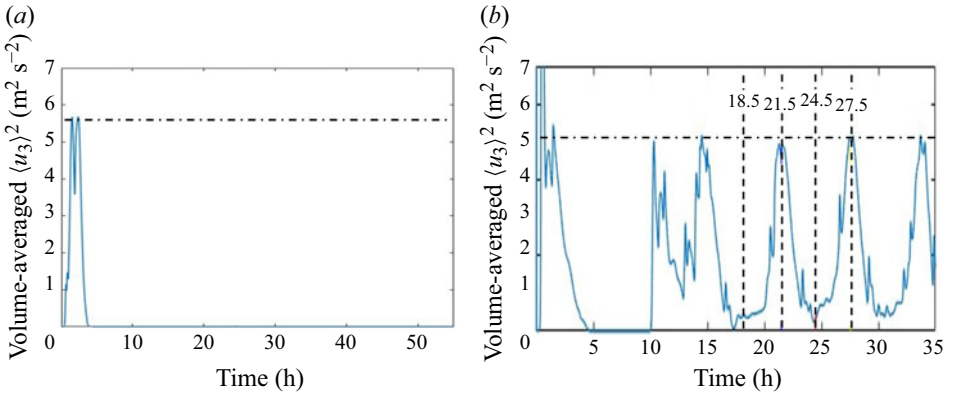

Figure 3. Time series of the volume-averaged vertical velocity variance during (*a*) weak-wave-forcing and (*b*) strong-wave-forcing conditions. The horizontal dashed–dotted lines denote the values of the depth-averaged vertical velocity variance obtained in corresponding simulations without tidal forcing characterised by steady-state LC.

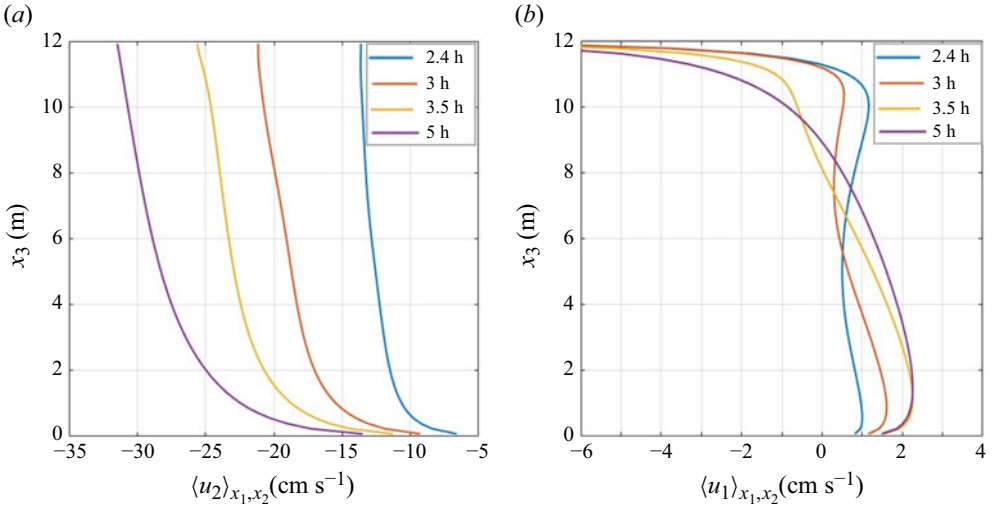

Figure 4. Vertical profiles of (*a*) along-shelf (crosswind) velocity, driven primarily by the tidal body force, and (*b*) cross-shelf (alongwind) velocity in the RANS simulation under weak-wave-forcing conditions, shown at selected tidal phases.

time, and in figure 4(*a*) in terms of depth profiles of the along-shelf velocity induced by the tidal body force. The LC which had formed within the first two hours of simulation (figure 2*a*), was fully suppressed as the tidal velocity reached its peak at approximately $t = 5$ h (figure 4*a*).

During the initial stage of the simulation with weak wave forcing, when LC was active, the downwelling and upwelling limbs of the cells induced elevated values of vertical velocity (figure 3*a*) and thus vertical mixing of momentum, resulting in reduced shear in the cross-shelf velocity (figure 4*b*, blue and red curves). As the LC was suppressed over time by the developing tidal current, the cross-shelf velocity profile showed greater vertical shear (figure 4*b*, yellow and purple curves).

Note that the depth profiles of the cross-shelf velocity in figure 4(*b*) represent an onshore-directed flow near the surface (characterised by negative velocity values) and

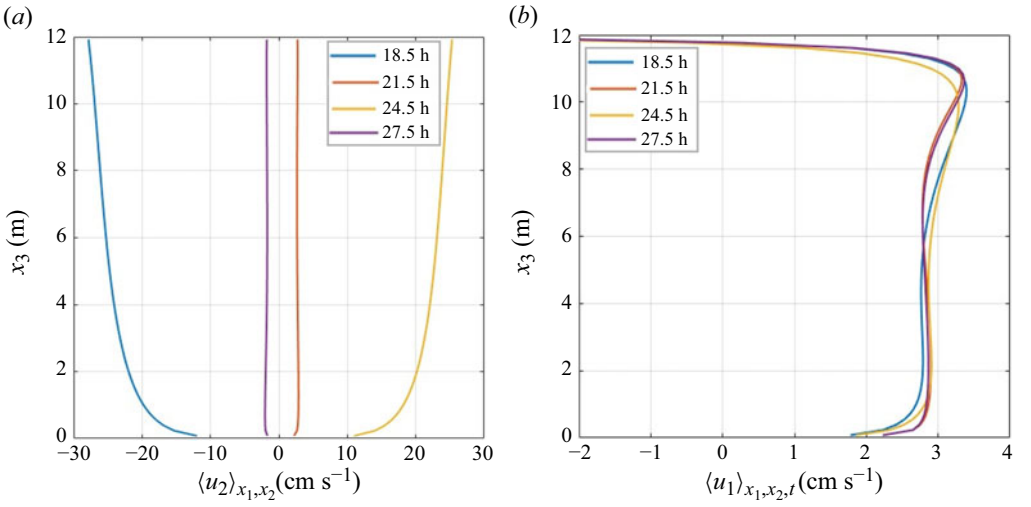

Figure 5. Vertical profiles of (*a*) along-shelf (crosswind) velocity, driven primarily by the tidal body force, and (*b*) cross-shelf (alongwind) velocity in RANS simulation under strong-wave-forcing conditions, shown at selected tidal phases.

a compensating undertow (characterised by positive velocity values), following the directions of the wind stress and the undertow body force, respectively, sketched in figure 1(*a*).

5.2. *Strong wave forcing*

Unlike the case with weak wave forcing, in the simulation with strong wave forcing, the oscillating tidal current and LC came into a time-dependent equilibrium characterised by periods when the cells and associated vertical velocity were at their strongest while the tidal velocity or energy was at its weakest and vice versa, indicative of a regulation of LC strength by the tides. This state is seen in figures 2(*e–h*), 3(*b*) and 5.

Times when cells are strongest or most coherent coincide with high vertical velocity variance and weak tidal velocity (energy) and vice versa. For example, for the strong-wave-forcing case, panels (*f*) and (*h*) in figure 2 show strong/coherent cells at $t = 21.5$h and $t = 27.5$ h, corresponding to times of high vertical velocity variance in figure 3(*b*) and weak tidal velocity in figure 5(*a*). Meanwhile, at $t = 18.5$h and $t = 24.5$ h, panels (*e*) and (*g*) of figure 2 show weak cell activity corresponding to low vertical velocity variance in figure 3(*b*) and strong tidal velocity in figure 5(*a*). The peak tidal current is able to reduce the vertical velocity variance by tenfold relative to its greatest value during weak tides.

At times of reduced LC activity (during peak tidal energy; figure 5*a*), the depth profiles of cross-shelf velocity in figure 5(*b*) exhibit only slightly greater shear compared with profiles at times of peak LC activity (during weak tidal energy). This suggests a lasting influence of previously established LC, which continues to enhance vertical momentum mixing even as tidal shear increases and temporarily suppresses active LC structures.

5.3. *Comparison with MVCO observations and baseline model*

Figure 6 compares the results of the RANS simulation with the predictions of the baseline model of Fewings *et al.* (2008) described in § 2 and their MVCO field measurements. As noted by Fewings *et al.* (2008), the field measurements were tidally averaged. Thus, for

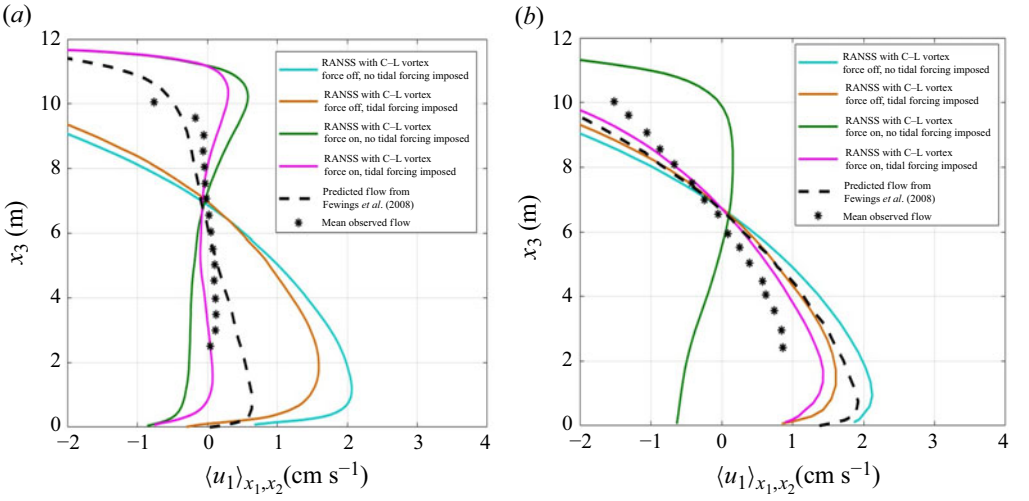

Figure 6. Tidally averaged vertical profiles of cross-shelf velocity during (*a*) strong-wave-forcing conditions and (*b*) weak-wave-forcing conditions represented via the C–L vortex force and the offshore pressure gradient, g_{utow}. The depth averages of the velocity profiles from $x_3 = 2.51$ m to $x_3 = 10.06$ m have been subtracted out. The u_τ flow component in the Fewings *et al.* (2008) (baseline) model (recall (2.1)) has been computed with the present RANSS (Reynolds-Averaged Navier–Stokes Simulations) code and the k–ϵ model for consistency of comparisons.

both the weak- and strong-wave-forcing cases, the RANS results with tidal forcing were averaged over a tidal period.

Furthermore, to facilitate a clearer comparison of vertical structure, the velocity profiles in figure 6 from the Fewings *et al.* (2008) field measurements and from the model simulations have been plotted with their respective depth averages removed. Although the water column extends from $x_3 = 0$ (bottom) to $x_3 = 12$ m (top or surface) in the models, the field measurements reported by Fewings *et al.* (2008) are only available from $x_3 = 2.51$ m to $x_3 = 10.06$ m due to instrument constraints, thus the depth averages for both observational and modelled data were obtained over this limited depth range.

The depth averages of the modelled profiles are determined by the body force g_{utow} in the RANS momentum equations and by (2.2) in the baseline model of Fewings *et al.* (2008). These approximations induce an error when comparing with field measurements (see Lentz *et al.* 2008) that is not investigated here, thus the mean of the velocity profiles is subtracted out in order to focus on the vertical structure of the velocity profiles.

Figures 6(*a*) and 6(*b*) compare the vertical profiles of cross-shelf velocity under strong wave forcing and weak wave forcing, respectively. The black stars represent the mean observed flow. The black dashed lines show the predicted flow by Fewings *et al.* (2008) through the baseline model.

The red and cyan lines show the results from the RANS simulation without the C–L vortex force with and without tidal forcing, respectively. In these cases with strong wave forcing (figure 6*a*), the velocity profiles deviate significantly from both the observed data and the predictions of the baseline model of Fewings *et al.* (2008). The profiles show excessive shear (plotted in figure 7*a*) relative to the field measurements and baseline model, as expected given the missing wave–current interaction (i.e. the absence of the C–L vortex force).

In figure 6(*a*), the magenta and green curves show the velocity profiles from the RANS simulation with the C–L vortex force set by strong waves, with and without the tidal force

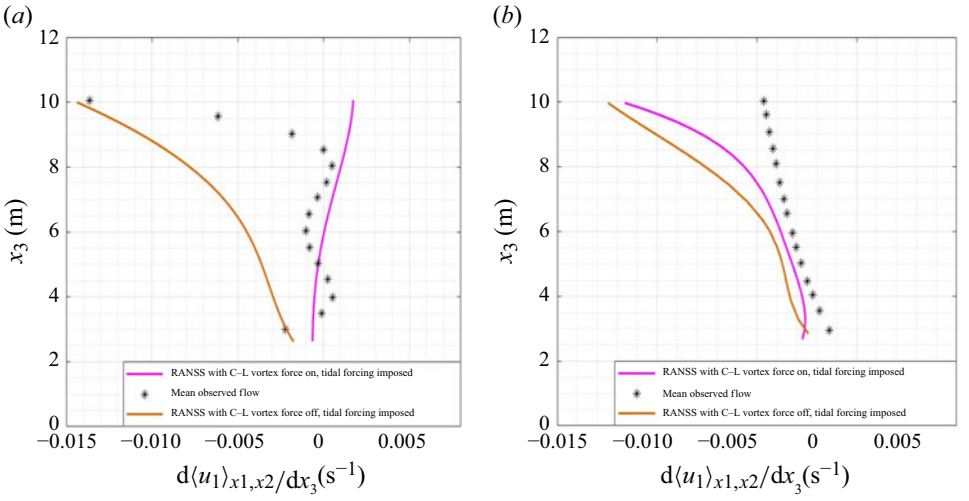

Figure 7. Vertical profiles of cross-shelf velocity shear for (*a*) strong-wave and (*b*) weak-wave cases from $x_3 = 2.51$ m to $x_3 = 10.06$ m, the depth range over which the field observations reported by Fewings *et al.* (2008) are available.

included, respectively. Remarkably, these curves closely follow the depth variation of both the baseline model and the observed data. In contrast, the RANS simulations without the C–L vortex force (red and cyan curves) show a significantly poorer match. Discrepancies near the surface may be attributed to missing effects such as wave breaking from the RANS simulation. Nevertheless, the inclusion of the C–L vortex force allows the model to more accurately predict the vertical distribution of cross-shelf momentum as a balance between the offshore wave-driven undertow and the onshore wind-driven surface flow. In figure 6(*a*), not much difference is observed between simulations with C–L vortex forcing with and without tidal forcing (magenta and green curves, respectively) indicative of the strength of LC in this case.

Figure 6(*b*) compares the vertical profiles of cross-shelf velocity under weak wave forcing. In this case, the influence of the tides in the RANS simulation is significant. Inclusion of the C–L vortex force without tides (green line) leads to excessive vertical mixing of momentum. The simulation including tidal forcing (magenta) shows that the tides are an important component, sufficiently strong to suppress the weaker LC leading to greater shear in the velocity profile, in closer agreement with the field measurements and the baseline model.

Comparing the tidally averaged cross-shelf velocity in figures 6(*a*), 6(*b*) and its vertical shear in figures 7(*a*), 7(*b*) for the RANS simulations with LC and tidal forcing shows that RANS simulation captures the significant reduction in vertical shear observed in the field measurements during strong wave forcing (panels *a*) (relative to weak wave forcing (panels *b*)). This supports our hypothesis that LC (present in the strong-wave case only) significantly impacts the vertical structure of cross-shelf momentum transport during periods of strong onshore winds and waves.

While the RANS simulation incorporates a tidal current in the along-shelf direction, field observations at MVCO reveal that the full tidal ellipse includes a significant cross-shelf component. Including this cross-shelf tidal forcing could enhance model–observation agreement, particularly under weak-wave conditions (figure 6*b*). However, this would

preclude the steady-state (subtidal) imposition of the offshore undertow body force driving the offshore subtidal mass flux balancing the onshore mass flux induced by the waves (recall (2.4)). Inclusion of a full tidal ellipse and other mechanisms that could be important in the weak-wave-forcing case, such as wave breaking and wave streaming, should be explored in the future.

Wave breaking, not represented in the present model, could influence the cross-shelf velocity and its vertical shear. The effects of wave breaking (which occurs in the field as white capping induced by strong wind forcing) are difficult to disentangle. Breaking directly produces an acceleration toward the shore in the surface layer (through a breaker force) yet also enhances vertical mixing that redistributes momentum vertically (Uchiyama *et al.* 2010), tending to slow the surface onshore (alongwind) flow and weaken the offshore flow near the bed. Without either effect in the present model, the simulated profile with C–L vortex and tidal forcing in figure 6(*b*) shows overly strong onshore velocity at the surface and overly strong offshore velocity near the bed compared with observations. Bottom wave streaming, also absent here, generates a near-bed onshore mean current in the oscillatory bottom boundary layer (Wang *et al.* 2020) and would act to slow the modelled offshore near-bottom flow and flatten the profile, potentially improving agreement with the observations.

In the strong-wave case, greater wave steepness would lead to more energetic and frequent breaking, with the same dual effects of surface acceleration and enhanced vertical mixing noted earlier. Under strong-wave forcing, the resolved LC is expected to dominate the reduction of vertical shear, and the modelled profile in figure 6(*a*) captures much of the observed structure. However, in the upper water column the modelled shear (figure 7*a*) is lower than observed, suggesting that near-surface mixing may be too vigorous. Part of this may stem from how the Stokes drift is specified: the present model uses a single bulk wave component (H_{sig} and T_w), which produces a deeper, more uniform profile than a spectrum-based calculation. A spectrum-based approach would yield larger Stokes drift near the surface and a faster decay with depth, focusing Langmuir production in the top layer and reducing mixing at depth. These changes could potentially help retain more of the observed near-surface shear.

6. Conclusion

Results from the present study support our initial hypothesis that the wave- and wind-driven LC is the source of the vertical mixing of undertow momentum observed by Fewings *et al.* (2008) in their data from MVCO during periods of strong onshore wind and wave forcing. Our Reynolds-averaged modelling framework shows that strong wave-driven LC sustains vertical mixing and reduces velocity shear throughout the tidal cycle, while tidal forcing can fully suppress LC, leading to increased shear when wave forcing is weak. These results are consistent with observed undertow profiles at MVCO, underscoring the necessity of resolving both the generation and disruption of LC for reliable predictions of cross-shelf momentum exchange. The findings highlight that the interplay between LC and tides fundamentally shapes inner-shelf flow dynamics, and future modelling efforts should incorporate these interactions to improve forecasts of coastal transport processes.

Funding. This work was made possible by the U.S. National Science Foundation (award 1756902).

Declaration of interests. The authors report no conflict of interest.

References

Fewings, M., Lentz, S.J. & Fredericks, J. 2008 Observations of cross-shelf flow driven by cross-shelf winds on the inner continental shelf. *J. Phys. Oceanogr.* **38** (11), 2358–2378.

Gargett, A., Wells, J., Tejada-Martinez, A.E. & Grosch, C.E. 2004 Langmuir supercells: a mechanism for sediment resuspension and transport in shallow seas. *Science* **306** (5703), 1925–1928.

Hasselmann, K. 1970 Wave-driven inertial oscillations. *Geophys. Astrophys. Fluid* **1** (3–4), 463–502.

Kukulka, T., Plueddemann, A.J., Trowbridge, J.H. & Sullivan, P.P. 2011 The influence of crosswind tidal currents on Langmuir circulation in a shallow ocean. *J. Geophys. Res. Oceans* **116** (C8), C08005.

Lentz, S.J. 1995 Sensitivity of the inner-shelf circulation to the form of the eddy viscosity profile. *J. Phys. Oceanogr.* **25** (1), 19–28.

Lentz, S.J., Fewings, M., Howd, P., Fredericks, J. & Hathaway, K. 2008 Observations and a model of undertow over the inner continental shelf. *J. Phys. Oceanogr.* **38** (11), 2341–2357.

Lentz, S.J. & Fewings, M.R. 2012 The wind-and wave-driven inner-shelf circulation. *Annu. Rev. Mar. Sci.* **4** (1), 317–343.

McWilliams James, C., Sullivan, P.P. & Moeng, C.-H. 1997 Langmuir turbulence in the ocean. *J. Fluid Mech.* **334**, 1–30.

Peñaloza-Gutierrez, J.J., Tejada-Martínez, A.E. & Boufadel, M.C. 2024 Reynolds-averaged Navier–Stokes simulation of nearshore Langmuir circulation and the formation of oil-particle aggregates. *Ocean Model.* **187**, 102306.

Perez, A.J., Cui, F., Peñaloza-Gutierrez, J., Zeidi, S., Sinha, N., Boufadel, M., Smith, C., Murphy, D.W. & Tejada-Martínez, A.E. 2021 Simulation of vertical dispersion of oil droplets by Langmuir supercells through a Reynolds-averaged eulerian formulation combined with Lagrangian particle tracking. *Ocean Eng.* **235**, 109043.

Savidge, D.K. & Gargett, A.E. 2017 Langmuir supercells on the middle shelf of the South Atlantic bight: 1. Cell structure. *J. Mar. Res.* **75**, 49–79.

Thorpe, S.A. 2004 Langmuir circulation. *Annu. Rev. Fluid Mech.* **36** (1), 55–79.

Uchiyama, Y., McWilliams, J.C. & Shchepetkin, A.F. 2010 Wave–current interaction in an oceanic circulation model with a vortex-force formalism: application to the surf zone. *Ocean Model.* **34** (1–2), 16–35.

Wang, P., McWilliams, J.C., Uchiyama, Y., Chekroun, M.D. & Yi, D.L. 2020 Effects of wave streaming and wave variations on nearshore wave-driven circulation. *J. Phys. Oceanogr.* **50** (10), 3025–3041.

Warner, J.C., Sherwood, C.R., Signell, R.P., Harris, C.K. & Arango, H.G. 2008 Development of a three-dimensional, regional, coupled wave, current, and sediment-transport model. *Comput. Geosci.* **34** (10), 1284–1306.